Journal of Materials Chemistry

Cite this: *J. Mater. Chem.*, 2012, **22**, 8048

www.rsc.org/materials

PAPER

Crystal structure characterization, optical and photoluminescent properties of tunable yellow- to orange-emitting $Y_2(Ca,Sr)F_4S_2:Ce^{3+}$ phosphors for solid-state lighting†

Yun-Chen Wu,[a] Yi-Chin Chen,[a] Teng-Ming Chen,*[a] Chi-Shen Lee,[b] Kuo-Ju Chen[c] and Hao-Chung Kuo[c]

Received 28th December 2011, Accepted 8th February 2012
DOI: 10.1039/c2jm16882k

In this study, a new efficient Ce^{3+}-doped fluorosulfide phosphor, $Y_2(Ca,Sr)F_4S_2:Ce^{3+}$, was obtained by using solid-state methods in a sealed silica ampoule. The synthesized $Y_2(Ca,Sr)F_4S_2:Ce^{3+}$ was characterized by powder X-ray diffraction and refined with Rietveld methods. $Y_2(Ca,Sr)F_4S_2:Ce^{3+}$ can be excited by blue light (440–470 nm) and shows yellow-to-orange broadband emission peaking at 553–590 nm with a quantum efficiency of 16–31%. Non-radiative transitions between Ce^{3+} ions in $Y_2CaF_4S_2:Ce^{3+}$ and $Y_2SrF_4S_2:Ce^{3+}$ hosts have also been demonstrated to be attributable to dipole–dipole interactions, and the critical distances were calculated to be 18.9 and 19.3 Å. The possible mechanism of the tunable luminescence properties was described on the basis of band structure calculations. In addition, a white LED device was fabricated by using $Y_2(Ca,Sr)F_4S_2:Ce^{3+}$ phosphor pumped with a 460 nm blue chip. The CRI value and CCT were measured to be 74–85 and 3500–8700 K, respectively, showing promising potential for solid-state lighting.

Introduction

In recent years, remarkable advancements have been made in the development of commercially realized efficient white light-emitting diodes (LEDs) for their merits of energy-efficient, life-durable and environmentally friendly characteristics.[1–3] The most common approach for white light relies on a blue LED chip and a blue-light excitable yellow phosphor, $(Y,Gd)_3(Al,Ga)_5O_{12}:Ce^{3+}$ (YAG:Ce).[4,5] Nevertheless, it is also characterized as cool white light because of its high correlated color temperature (CCT) of >8000 K, and poor color rendering index (CRI, *Ra*) of 70–75.[4,6–8] To improve the mentioned problems, Ce^{3+} or Eu^{2+}-doped sulfide phosphors were reported for their applicability of generating white light, because they show strong blue absorption and green- to red-emitting color.[9] Jia and Wang summarized a series of rare-earth doped alkali-earth sulfide, *AE*S:Ce^{3+} or Eu^{2+} (*AE* = Ca, Sr), which is suitable for blue LED pumping.[10] A similar type of white light was achieved by Guo *et al.* using (Ca,Sr)S:Eu^{2+}, Ln^{3+} (*Ln* = La, Pr–Nd, Sm–Yb). A relatively high CRI value of 82–92 and low CCT of 3600–4800 K were reported.[11–13] However, this class of binary materials shows a relatively strong thermal quenching and a limited stability with moisture. Recently, several ternary sulfide phosphors were reported in order to ameliorate the aforementioned drawbacks, *e.g.*, Ce^{3+} or Eu^{2+}-doped thiosilicates and thiogallates.[14,15] Accordingly, it is essential to develop a new sulfide phosphor which can be effectively excited by the blue light and also possess better chemical property.[16] The Ce^{3+} emission usually consists of an asymmetric broad band due to the parity allowed characteristics of the transition between the lowest crystal field components' 5d excited state and the 4f ground state ($^2F_{7/2}$ and $^2F_{5/2}$), and can be varied from ultraviolet to yellow in its emitting color, depending on the different host lattices.[17–19] In this study, we present a new Ce^{3+}-doped mixed-anion fluorosulfide $Y_2(Ca,Sr)F_4S_2:Ce^{3+}$ phosphor. The quaternary $Ln_2AEF_4S_2$ (*Ln* = Ce, Sm, Eu, Yb; *AE* = Ca, Sr) halogensulfide material has been originally recognized as a ceramic/glass pigment, however, its luminescence property has yet to be investigated.[20–22] In $Y_2(Ca,Sr)F_4S_2$ host lattice, the Ce^{3+} is coordinated by both fluoride and sulfide anion. With low phonon energy in fluoride anion and strong covalency in sulfide anion, the efficient emission due to the minor quenching process from multi-phonon relaxation and longer wavelength emission for Ce^{3+} is expected in $Y_2(Ca,Sr)F_4S_2:Ce^{3+}$.[23,24] In this work, we report on the luminescence properties of $Y_2CaF_4S_2:Ce^{3+}$ and it exhibits an absorption band in the blue region with a broad orange emission peaking at 590 nm, making it an appropriate candidate for our pursuit of a new phosphor component for

[a]*Phosphors Research Laboratory, Department of Applied Chemistry and Institute of Molecular Science, National Chiao Tung University, Hsinchu 30010, Taiwan. E-mail: tmchen@mail.nctu.edu.tw*
[b]*Department of Applied Chemistry and Institute of Molecular Science, National Chiao Tung University, Hsinchu 30010, Taiwan*
[c]*Semiconductor Laser Technology Laboratory, Department of Photonics, National Chiao Tung University, Hsinchu 30010, Taiwan*

† Electronic supplementary information (ESI) available: EDX spectra, SEM image, XRD patterns, structural parameters, and decay curves. See DOI: 10.1039/c2jm16882k

white LED. We also thoroughly studied the Sr^{2+} substitution in $Y_2CaF_4S_2$:Ce^{3+} in an attempt to realize the effect of compositional modification on spectroscopic properties. Furthermore, we utilized the structural parameters of $Y_2CaF_4S_2$, $Y_2SrF_4S_2$, $Ce_2CaF_4S_2$, and $Ce_2SrF_4S_2$ to calculate their densities of state (DOS), which in turn allowed us to investigate distribution of energy levels in fluorosulfide systems and to propose their working luminescence mechanisms. Finally, temperature dependence and the LED device using $Y_2(Ca,Sr)F_4S_2$:Ce^{3+} phosphors with blue chip were investigated to demonstrate the applicability of the $Y_2(Ca,Sr)F_4S_2$:Ce^{3+} phosphor as a color conversion material.

Experimental section

Synthesis

The polycrystalline samples of $Y_{2-x}Ce_xCaF_4S_2$, $Y_{2-x}Ce_xSrF_4S_2$, and $Y_{1.98}Ce_{0.02}Ca_{1-y}Sr_yF_4S_2$ were prepared by solid-state reactions using YF_3 (Alfa), CaF_2 (Aldrich), SrF_2 (Aldrich), CaS (Alfa), SrS (Alfa), Y_2S_3 (Alfa), and CeF_3 (Aldrich) as raw materials. The stoichiometric amounts of the starting materials were thoroughly mixed and loaded into Al_2O_3 tubing, which was transferred into a vertically positioned quartz ampoule, fully evacuated to 10^{-3} torr and sealed off. The quartz ampoule was heated to 900–1000 °C for 8–12 h and then cooled down slowly to room temperature. The obtained product was then annealed at 500–600 °C for 2–8 h under 1–5% H_2/Ar atmosphere.

Characterizations

The phase purity of the reaction product was analyzed by powder X-ray diffraction (XRD) using a Bruker AXS D8 advanced automatic diffractometer with Cu Kα radiation (λ = 1.5418 Å, 40 kV × 40 mA). The powder diffraction data were subjected to analysis by a computer software General Structure Analysis System (GSAS) package.[25] Refined structure parameters comprised overall scale factors, lattice parameters, and fractional coordinates. The morphology and energy-dispersive X-ray spectroscopy (EDX) spectrum were measured by a JEOL JSM-7401F conventional thermal field-emission scanning electron microscope. The diffuse reflection spectra were measured with a Hitachi 3010 double-beam ultraviolet-visible (UV-Vis) spectrometer (Hitachi Co., Tokyo, Japan) equipped with a ø60 mm integrating sphere. The photoluminescence (PL) and photoluminescence excitation (PLE) spectra were recorded with a Spex Fluorolog-3 spectrofluorometer (Jobin Yvon Inc/specx) equipped with a 450 W Xe lamp and analyzed by a Jobin-Yvon spectrometer HR460 with a multichannel charge-coupled device detector. The Commission Internationale de l'Eclairage (CIE) chromaticity coordinates were determined by a Laiko DT-100 color analyzer equipped with a CCD detector (Laiko Co., Tokyo, Japan). The program Linear Muffin Tin Orbital (LMTO)[26,27] was used to calculate the electronic structures of $Y_2CaF_4S_2$, $Y_2SrF_4S_2$, $Ce_2CaF_4S_2$, and $Ce_2SrF_4S_2$. The density functional theory is used with the local density approximation (LDA).[28] The integration in k point is performed by an improved tetrahedron method on a grid of 40 × 40 × 40 k points for $Y_2CaF_4S_2$ and $Ce_2CaF_4S_2$, and 16 × 16 × 16 k points for $Y_2SrF_4S_2$ and $Ce_2SrF_4S_2$ of the first Brillouin zone. The crystallographic parameters used for the calculation were derived from the GSAS refinement data. The final results from the calculations are examined to obtain the electronic properties, such as the band structure, total and partial densities of states. The phosphor-converted white LED devices were fabricated using commercial blue InGaN-based LED (λ_{max} = 460 nm) with an intimate mixture of as-synthesized phosphors and silicone resin. Electroluminescence (EL) spectra were recorded at a forward-current and measured by using a SphereOptics integrating sphere with LED measurement starter packages (Onset, Inc.).

Results and discussion

Structural characterizations and crystallographic parameters of the $Y_{1.98}Ce_{0.02}AEF_4S_2$ (AE = Ca, Sr) phosphors

The Rietveld refinements were accomplished in order to obtain the detailed crystal information about $Y_{1.98}Ce_{0.02}AEF_4S_2$ (AE = Ca, Sr) and ensure the purity of the samples phase. The initial structural model was first built with crystallographic data of isotypic single-crystal Eu_2(III)Eu(II)F_4S_2.[22] According to the similarity of effective cationic radii in the same coordination environment,[29] the Eu^{3+} can be substituted by the Y^{3+} ion; also, the Eu^{2+} can be substituted by Ca^{2+} and Sr^{2+} ions. Therefore, the title hosts $Y_2CaF_4S_2$ and $Y_2SrF_4S_2$ (hereafter referred to as YCFS and YSFS) were demonstrated. The fractional occupancies of each component atom were adjusted to the nominal stoichiometry. Fig. 1 presents the Rietveld refinement results for $Y_{1.98}Ce_{0.02}CaF_4S_2$ (YCFS:Ce^{3+}) and $Y_{1.98}Ce_{0.02}SrF_4S_2$ (YSFS:Ce^{3+}) from the observed XRD patterns, indicating the final converged weighted-profile of R_{wp} = 6.8% and 4.96%, respectively. Both structures were found to crystallize tetragonally in the space group $I4/mmm$ (no. 139) with Z = 2. In the crystal structure of YCFS and YSFS, both Ce and Y atoms occupy only the 4e position site, as presumed, due to the inability of Ce^{3+} ions achieving the divalent oxidation state. Furthermore, the 2b site is fully occupied by Ca or Sr atoms, the 4e site is fully occupied by S atoms and the 16n site is estimated to be half-filled by F atoms. The final refined structural parameters, selected atomic distances, and bond angles of YCFS:Ce^{3+} and YSFS:Ce^{3+} are summarized in Tables 1 and 2. The grain size and morphology of YCFS:Ce^{3+} particles were characterized by SEM, which indicates that the as-synthesized phosphor was composed of many irregular granular microcrystals with an average size of ~5 to 10 μm. The nominal stoichiometry was also verified accurately by EDX measurement (see Fig. S1 in the ESI†).

Fig. 2 shows the exact 1 × 1 × 1 unit cell crystal structure of the YCFS lattice viewed from the [010] and the Y atomic sites along with their corresponding neighboring atoms from the refined result. The structure of YCFS can be depicted as an ordered intergrowth YF_4S_5/CaF_8/YF_4S_5 polyhedra layer structure similar to the $Ln_3F_4S_2$-family (Ln = Eu, Yb),[20,22] which was composed of one *fluoride*-analogous (AE = Ca, Sr, Ba) sheet and two PbFCl-type sheets along the c-axis repeat. The coordination polyhedron YF_4S_5 is comprised of five S, four F atoms and one Y atom situated in the center of the monocapped square antiprism (CN = 9). According to the point charge theory, the five degenerate 5d orbitals of Ce^{3+} are regarded as having split into

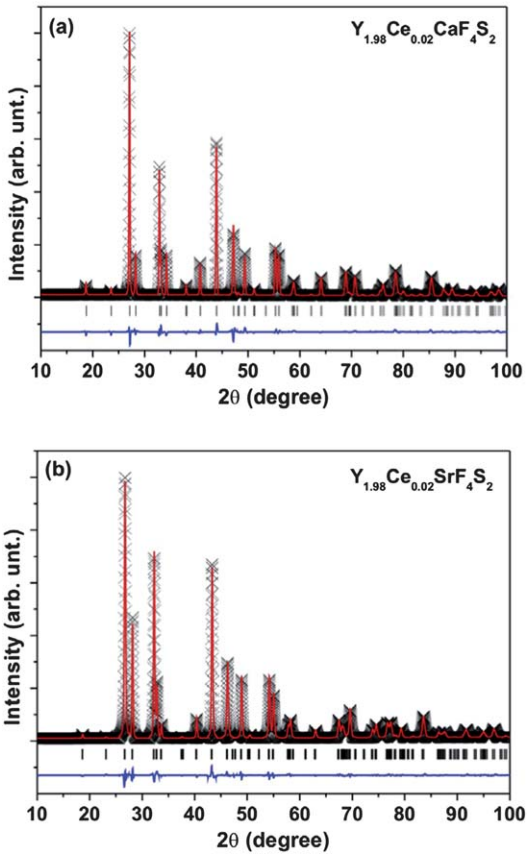

Fig. 1 XRD profiles for Rietveld refinement results of (a) $Y_{1.98}Ce_{0.02}CaF_4S_2$ and (b) $Y_{1.98}Ce_{0.02}SrF_4S_2$. Observed intensities (cross), calculated patterns (red line), Bragg positions (tick mark), and difference plot (blue line) are presented.

five distinct d levels in the increasing order of energy levels d_{x2-y2}, d_{z2}, d_{yz}, d_{xz}, and d_{xy} in C_{4v} symmetry.[19,30] The crystal splitting of 5d levels can be further changed by the geometrical translation, that is, the so-called nephelauxetic effect. The isotropic volume contraction strengthens crystal field splitting, accordingly lowering the lowest-lying 5d level and altering the excitation and emission wavelength, whereas isotropic volume expansion produces the opposite effect. In our case, the variations in PLE/PL spectra coupled with changing Ca/Sr substitutional ratio were observed; this part is to be discussed later.

Spectroscopic study of $Y_2AEF_4S_2:Ce^{3+}$ (AE = Ca, Sr)

Fig. 3 shows the diffuse reflection spectrum of as-synthesized polycrystalline YCFS and the PLE/PL spectra of YCFS:Ce^{3+}. For the YCFS host, the diffuse reflection spectrum shows a status of high reflection in the wavelength ranging from 400 to 800 nm and decreasing intensity from 250 to 400 nm. The Kubelka–Munk absorption coefficient (K/S) relation was used to calculate the absorption edge from the measured reflectance (R) of the YCFS host:[31]

$$\frac{K}{S} = \frac{(1-R)^2}{2R} \quad (1)$$

Table 1 Crystal structural data and isotropic displacement parameters of $Y_{1.98}Ce_{0.02}CaF_4S_2$ and $Y_{1.98}Ce_{0.02}SrF_4S_2$ crystal systems from Rietveld refinement[a]

Formula			$Y_{1.98}Ce_{0.02}CaF_4S_2$			
Lattice parameters			a = 384.97(5), c = 1891.53(4), V = 280.33(6)			
R_{wp}			6.8%			
R_p			4.92%			
χ^2			2.02			
Atom	Wyck.	x/a	y/b	z/c	S.O.F.	U
Y	4*e*	0	0	0.1563(2)	0.982	0.0071(2)
Ca	2*b*	0	0	0.5	1.005	0.0081(2)
S	4*e*	0.5	0.5	0.1933(8)	0.997	0.0093(6)
F	16*n*	0	0.4997(2)	0.0674(2)	0.478	0.0204(2)
Ce	4*e*	0	0	0.1563(2)	0.018	0.0017(2)
Formula			$Y_{1.98}Ce_{0.02}SrF_4S_2$			
Lattice parameters			a = 393.46(5), c = 1907.23(4), V = 295.25(4)			
R_{wp}			4.96%			
R_p			3.57%			
χ^2			0.79			
Atom	Wyck.	x/a	y/b	z/c	S.O.F.	U
Y	4*e*	0	0	0.1569(2)	0.981	0.0066(2)
Sr	2*b*	0	0	0.5	0.987	0.0112(2)
S	4*e*	0.5	0.5	0.1938(8)	0.998	0.0109(8)
F	16*n*	0	0.5	0.0659(2)	0.49	0.0106(2)
Ce	4*e*	0	0	0.1565(2)	0.019	0.015(2)

[a] Tetragonal; space group: *I*4/*mmm* (no. 139); lattice parameters: a and c in pm, V in 10^6 pm^3; $\alpha = \beta = \gamma = 90°$; T = 298 K; Z = 2; Cu Kα, λ = 1.5418; total reflections = 5375; Site Occupancy Fraction (S.O.F.); U in Å^2.

Table 2 Selected interatomic bond distances[a] of $Y_{1.98}Ce_{0.02}CaF_4S_2$ and $Y_{1.98}Ce_{0.02}SrF_4S_2$

$Y_{1.98}Ce_{0.02}CaF_4S_2$		$Y_{1.98}Ce_{0.02}SrF_4S_2$	
(Y/Ce)–S	281.08(3) (4×)	(Y/Ce)–S	286.94(2) (4×)
(Y/Ce)–S	284.63(7) (1×)	(Y/Ce)–S	284.71(3) (1×)
(Y/Ce)–F	255.38(3) (4×)	(Y/Ce)–F	262.41(1) (4×)
Ca–F	255.58(3) (4×)	Sr–F	233.45(1) (4×)
Ca–F	255.58(3) (4×)	Sr–F	233.45(1) (4×)

[a] Bond distances in pm.

where K represents the absorption coefficient, S represents the scattering coefficient, and R represents the reflectivity. The fundamental band gap energy of the YCFS was calculated to be approximately 3.39 eV by extrapolation. The observed color of YCFS is light yellow, which then turns yellow with doping Ce^{3+} ions. For YCFS:Ce^{3+}, a typical PLE and PL spectra were observed. In order to study the Ce 5d and 4f energy levels in YCFS:Ce^{3+}, we first discriminated each preferential site for Ce^{3+} dopants in YCFS:Ce^{3+}. Comparing the emission bands in YCFS:Ce^{3+} and $CaF_2:Ce^{3+}$,[19,32–34] both have a nearly identical chemical environment around the Ca^{2+} ion, *viz.*, the same coordination number of eight, same atom symmetry (D_{4h}) and a similar Ca–F bond distance, but occur with different emission wavelengths, widths and Stoke shifts. This suggests that the

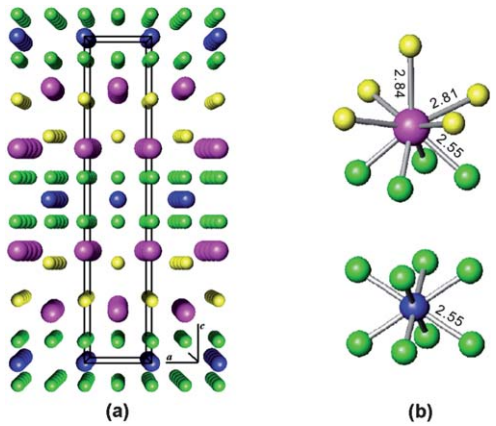

Fig. 2 (a) Schematic unit cell crystal structure of $Y_{1.98}Ce_{0.02}CaF_4S_2$ and (b) coordination environment around YF_4S_5 and CaF_8. Pink, blue, green, and yellow spherical balls describe Y/Ce, Ca, F, and S atoms.

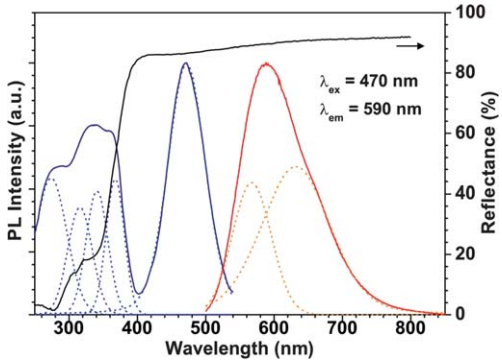

Fig. 3 Diffuse reflection spectrum of $YCaF_4S_2$ host and PLE/PL spectra of $Y_{1.98}Ce_{0.02}CaF_4S_2$. The deconvolutions of excitation and emission bands are illustrated as dashed lines.

orange emission is originated from the substitution of the Ce^{3+} ion for the Y^{3+} ion rather than the Ca^{2+} ion. Since the Ce^{3+} emission can be only observed on the 4*e* site, the asymmetric emission band in the PL spectrum was fitted into two Gaussian curves centering respectively at 567 and 632 nm, ascribed to the transitions from the lowest $5d_{x2-y2}$ level to the two $^2F_{7/2}$ and $^2F_{5/2}$ ground states of the Ce^{3+} ions.[35,36] Then, the energy gap between $^2F_{7/2}$ and $^2F_{5/2}$ associated with spin-orbit splitting was calculated to be 1814 cm^{-1} (usually ~2000 cm^{-1}).[19] On the other hand, the PLE spectrum was characterized by two main excitation bands in the UV-vis range: one band in UV is centered at ~340 nm (range from 250 to 400 nm) with two shoulders at 275 and 370 nm and another band in visible is centered at ~470 nm (range from 420 to 530 nm). The excitation band in the UV range overlapped partially with the host absorbance; however, different Ce^{3+} concentrations can still affect the intensity and thereby confirm the transition from 4f to 5d states of Ce^{3+}. The PLE spectrum can be further decomposed into several Gaussian functions at ~270, 308, 339, and 368 nm, which are found to be correlated with the $4f^1 \rightarrow 4f^05d^1$ (b_2, *e* and a_1) transitions and the excitation band at ~472 nm is owing to the $4f^1 \rightarrow 4f^05d^1$ (b_1) transitions. The center of gravity (COG) of the excitation bands is calculated to be approximately 29.47×10^3 cm^{-1} (3.66 eV). Also, we can estimate the crystal field splitting (CFS) to be about 15.85×10^3 cm^{-1} (1.97 eV) based upon the highest and lowest absorption bands in the PLE spectrum. Depending upon the lowest excitation and the higher emission energy, the Stoke shift is obtained to be 3550 cm^{-1} (440 meV).[34]

Fig. 4 shows the PLE and PL spectra of $Y_{2-x}Ce_xCaF_4S_2$ and $Y_{2-x}Ce_xSrF_4S_2$ (x = 0.01, 0.02, 0.04, and 0.06). The relative intensity of both the PLE and PL spectra varies in accordance with different doped Ce^{3+} concentrations, and an optimal value, also called critical concentration (x_c), was obtained for $x = 0.02$ (*ca.* 1 mol%). Because each activator ion is introduced solely into one site, there is on average one activator per V/x_cN when considering the concentration quenching caused by energy transfer mechanisms, such as exchange interaction, radiation reabsorption, or multipole–multipole interaction.[37] The critical transfer distance (R_c) is equal to approximately twice the radius of a sphere with the volume:[37,38]

$$R_c \approx 2\left(\frac{3V}{4\pi x_c N}\right)^{\frac{1}{3}} \quad (2)$$

where V represents the volume of unit cell, x_c represents the critical concentration, and N represents the number of total Ce^{3+} sites in the unit cell. According to the crystal structure of the YCFS:Ce^{3+} and YSFS:Ce^{3+} compounds, R_c values are reckoned to be 18.8 and 19.2 Å. If the rapid migration of Ce^{3+} ions occurs, quenching tends to be proportional to the Ce^{3+} concentration; this is not observed in PL spectra since the PLE and PL spectra do not overlap very well and the exchange interaction generally takes place in forbidden transition (the R_c is typically ~5 Å). Therefore, based on the Dexter theory, we can infer that the non-radiative concentration quenching between the two nearest Ce^{3+} centers occurs *via* electric multipolar interactions.[39] For the emission intensity per activator concentration, the following equation can be described:[40–42]

$$\frac{I}{x} = \frac{k}{1+\beta(x)^{\theta/3}} \quad (3)$$

where I represents the quenching intensity; x represents the Ce^{3+} concentration; k and β represent constants for individual electric multipolar interactions; and θ = 6, 8, 10 correlate correspondingly to the dipole–dipole, dipole–quadrupole, and quadrupole–quadrupole interactions. Assuming that $\beta(x)^{\theta/3} \gg 1$, the correlation between $\log(I/x)$ with $\log(x)$ can be fitted linearly within the PL spectra of $Y_{2-x}Ce_xCaF_4S_2$ and $Y_{2-x}Ce_xSrF_4S_2$ (x = 0.02, 0.04, and 0.06) and the values of θ are determined to be 6.12 and 5.67 from the slopes (θ/3). In particular, the calculated value for both $Y_{2-x}Ce_xCaF_4S_2$ and $Y_{2-x}Ce_xSrF_4S_2$ is close to 6, which implies that the concentration quenching mechanisms in Ce^{3+} emission are strongly accounted for in the dipole–dipole interaction. For the electric dipole–dipole mechanism, the transfer probability can be defined:[37]

$$P^{DD}_{Ce-Ce} = 0.63 \times 10^{28} \frac{Q_A}{\tau_{SO} R^6_{Ce-Ce} E^4} \int F_S(E) F_A(E) dE \quad (4)$$

where $Q_A = 4.8 \times 10^{-16} f_d$ is the absorption cross-section of Ce^{3+}; $f_d \approx 0.01$ is the electric dipole oscillator strength for Ce^{3+}; E (in eV) is the maximum energy of spectral overlap; integrated area represents the spectral overlap between the normalized

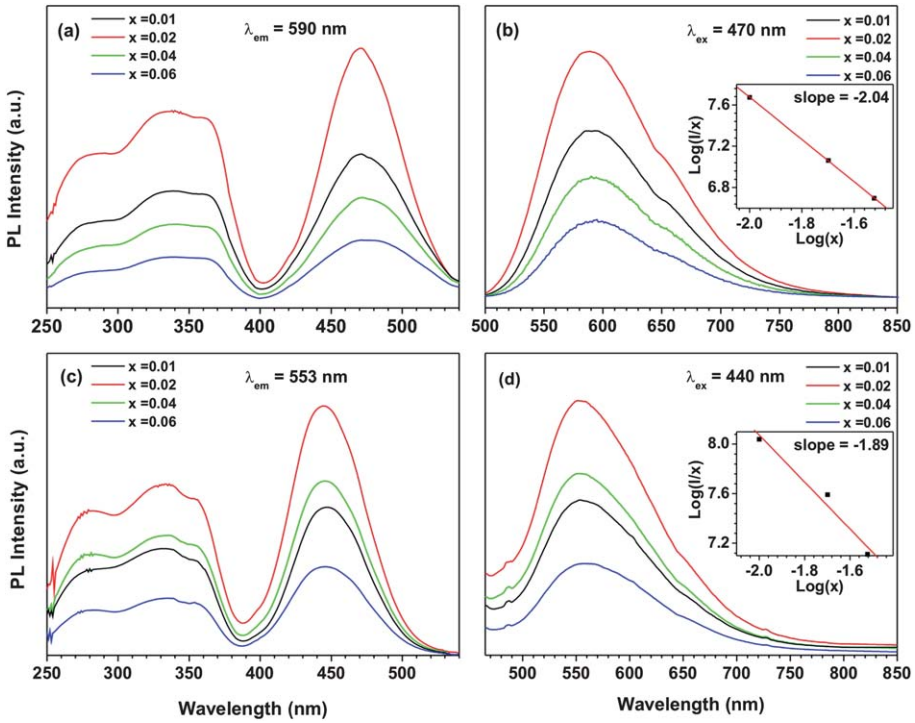

Fig. 4 The PLE and PL spectra of $Y_{2-x}Ce_xCaF_4S_2$ (a and b) and $Y_{2-x}Ce_xSrF_4S_2$ (c and d) with different Ce^{3+} concentrations, x. The insets show the correlation between $\log(I/x)$ with $\log(x)$.

shapes of Ce^{3+} emission $F_S(E)$ and Ce^{3+} excitation $F_A(E)$, and it is estimated to be about 0.0481 and 0.0739 eV^{-1}. The critical distance R_c of energy transfer between Ce^{3+} is defined as the distance for which the probability of transfer equals the probability of radiative emission of Ce^{3+}, *i.e.*, the distance for which $P_{Ce-Ce}\tau_{SO} = 1$. Therefore, R_c can be calculated using the following equation:[40]

$$R_c^6 = 0.63 \times 10^{28} \frac{Q_A}{E^4} \int F_S(E) F_A(E) dE \quad (5)$$

The R_cs of energy transfer between Ce^{3+} in YCFS:Ce^{3+} and YSFS:Ce^{3+} were calculated to be about 18.98 and 19.34 Å, which is close to that of the value obtained from concentration spectra.

With increasing Ce^{3+} concentration, the wavelength of excitation and emission bands remains practically unchanged for both materials. In contrast, the excitation and emission bands in the visible region denote an obvious blueshift in YSFS:Ce^{3+} compared to YCFS:Ce^{3+}, which is related to the changed crystal field strength. The model that describes the crystal field splitting on account of the shape and size of the polyhedron can be determined in the following relationship:[42,43]

$$D_q = \frac{3Ze^2r^4}{5R^5} \quad (6)$$

where D_q represents crystal field strength, Z represents the valence of the anion ligand, e represents the charge, r represents radius of frontier d wave function, and R represents the bond length between a center ion and ligands. The substitution of Ca^{2+} ion is employed by isovalent substituent Sr^{2+} ion, with both ions known to be compatible with the phosphor host. Here, we note

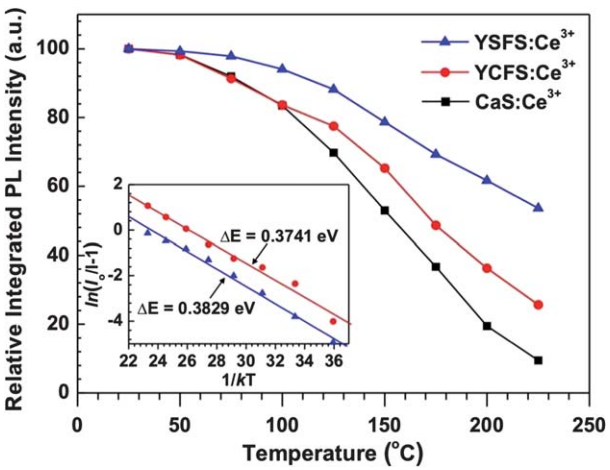

Fig. 5 Temperature-dependent PL intensity of commercial CaS:Ce^{3+}, $Y_{1.98}Ce_{0.02}CaF_4S_2$, and $Y_{1.98}Ce_{0.02}SrF_4S_2$. The inset shows the fitted PL intensity and the calculated thermal activation energy (ΔE) as a function of temperature.

that the above substitution leads to size expansion of the lattice volume, which is induced by larger Sr^{2+} ionic size, thus changing four Ce–S and four Ce–F bonds to 286.94 and 262.41 pm within the internal YF_4S_5 polyhedra. The bond lengths of apical Ce–S, 284.63 and 284.71 pm are almost the same in YCFS:Ce^{3+} and YSFS:Ce^{3+} (Table 2). In such cases, the Ce^{3+} ion experiences a weaker crystal field splitting due to the expansion of YF_4S_5 polyhedra in YSFS:Ce^{3+}; therefore, it is reasonable that the blueshift PLE and PL spectra are observed. The full width at half

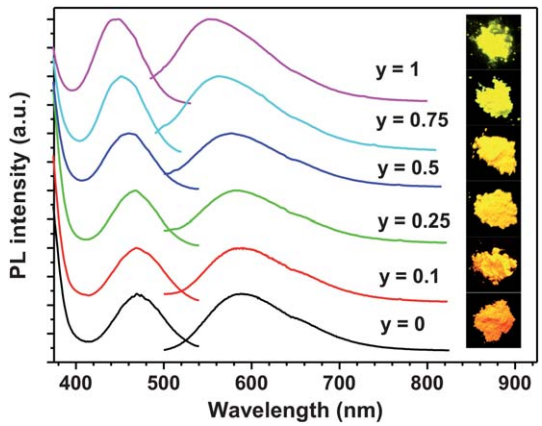

Fig. 6 Excitation (monitored at 550–590 nm) and emission (λ_{ex} = 440–470 nm) spectra of $Y_{1.98}Ce_{0.02}CaF_4S_2$, $Y_{1.98}Ce_{0.02}(Ca_{1-y}Sr_y)F_4S_2$ (y = 0.1, 0.25, 0.5, and 0.75), and $Y_{1.98}Ce_{0.02}SrF_4S_2$. The inset shows $Y_{1.98}Ce_{0.02}CaF_4S_2$, $Y_{1.98}Ce_{0.02}(Ca_{1-y}Sr_y)F_4S_2$ (y = 0.1, 0.25, 0.5, and 0.75), and $Y_{1.98}Ce_{0.02}SrF_4S_2$ photos taken under 365 nm excitation.

Table 3 Spectral and structural parameters for $Y_{1.98}Ce_{0.02}CaF_4S_2$, $Y_{1.98}Ce_{0.02}(Ca_{1-y}Sr_y)F_4S_2$ and $Y_{1.98}Ce_{0.02}SrF_4S_2$ phosphors; λ_{ex}, λ_{em} and average interatomic distances of Ce–S and Ce–F[a]

Sample	Composition	λ_{ex}	λ_{em}	d_{Ce-S}	d_{Ce-F}
YCFS:Ce^{3+}	$Y_{1.98}Ce_{0.02}CaF_4S_2$	471	590	281.1	255.4
YCSFS-0.1:Ce^{3+}	$Y_{1.98}Ce_{0.02}Ca_{0.9}Sr_{0.1}F_4S_2$	470	588	281.9	255.9
YCSFS-0.25:Ce^{3+}	$Y_{1.98}Ce_{0.02}Ca_{0.75}Sr_{0.25}F_4S_2$	467	578	283.2	258
YCSFS-0.5:Ce^{3+}	$Y_{1.98}Ce_{0.02}Ca_{0.5}Sr_{0.5}F_4S_2$	461	575	285	260
YCSFS-0.75:Ce^{3+}	$Y_{1.98}Ce_{0.02}Ca_{0.25}Sr_{0.75}F_4S_2$	451	563	285.9	261
YSFS:Ce^{3+}	$Y_{1.98}Ce_{0.02}SrF_4S_2$	440	553	286.9	262.4
	CaS:Ce^{3+}	456	502–560		

[a] Wavelength in nm; average interatomic distances in pm.

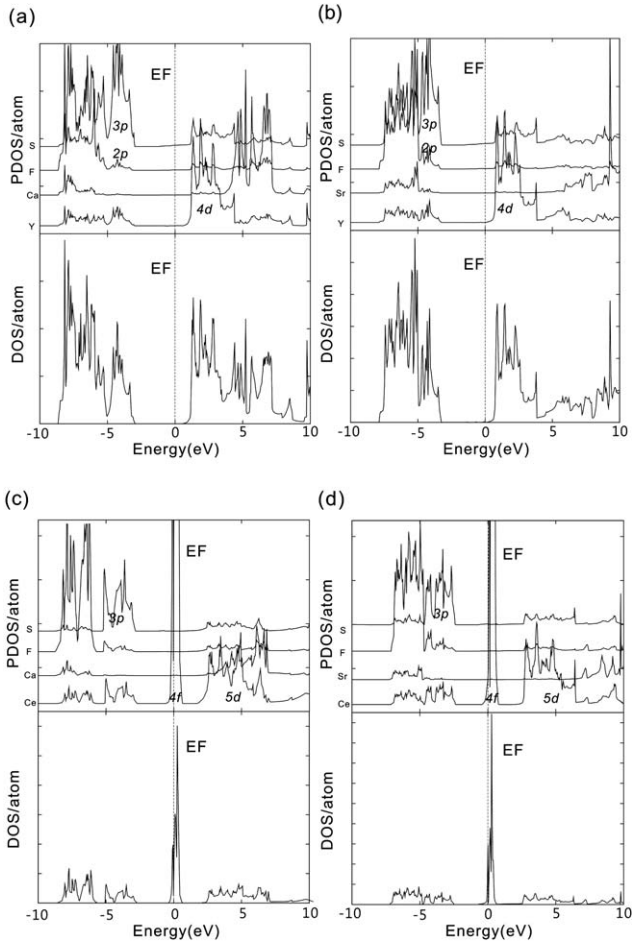

Fig. 7 The total (DOS) and partial (PDOS) density of states and the projected DOS curves for (a) YCFS, (b) YSFS, (c) CeCFS, and (d) CeSFS.

maximum (FWHM) of the emission bands are both found to be larger than 100 nm. The results depict that both Ce^{3+}-doped $Y_2CaF_4S_2$ and $Y_2SrF_4S_2$ fluorosulfides can achieve good color rendering when incorporated in phosphor-converted white LED.

Fig. 5 shows the temperature-dependent PL intensity of CaS:Ce^{3+}, YCFS:Ce^{3+}, and YSFS:Ce^{3+} in the range of 25 °C to 225 °C. The PL intensity of all samples is found to be diminished as compared to that observed at room temperature. This is due to the increasing thermal energy which ionized the electrons from the lowest state of the conduction band. Depending on the PL results, the intensity of fluorosulfide is comparable to (or even more stable than) that of binary sulfides. The introduction of F atoms into the sulfide host lattice may lower the extent of thermal quenching as a result of the softer phonon modes.[30] To investigate the origin of temperature dependent emission intensity, the activation energy (E_a) of the electrons being excited from the 4f level to the lowest 5d level of Ce^{3+} can be described in the following equation:[44,45]

$$I(T) = \frac{I_0}{1 + A\exp\left(-\frac{E_a}{kT}\right)} \quad (7)$$

where I_0 and $I(T)$ represent the PL intensity at room temperature and any temperature, respectively; k represents the Boltzmann constant. The values of E_a for YCFS:Ce^{3+} and YSFS:Ce^{3+} are estimated to be 0.3741 and 0.3829 eV, respectively. The YSFS:Ce^{3+} shows higher activation energy characteristics compared to those of YCFS:Ce^{3+}. The results indicated that the fluorosulfide could be a potential phosphor for solid-state lighting.

Tunable optical properties of $Y_{1.98}Ce_{0.02}(Ca_{1-y}Sr_y)F_4S_2$ phosphors

To design a potentially compatible phosphor for a blue LED chip, the appropriate excitation band should be as close to 460 nm as possible. On the basis of the PLE results, the Ca/Sr ratio can be varied in order to obtain the desired excitation and emission wavelength of fluorosulfide phosphors. In all compositions, *viz.*, YCFS:Ce^{3+}, YCSFS-y:Ce^{3+} (y = 0.1, 0.25, 0.5, and 0.75), and YSFS:Ce^{3+}, the single-phase samples were obtained in the same synthetic condition. The Sr^{2+} ion substitution for Ca^{2+} causes the shift of diffraction peaks to a lower angle position, which is in agreement with the refined data. The lattice

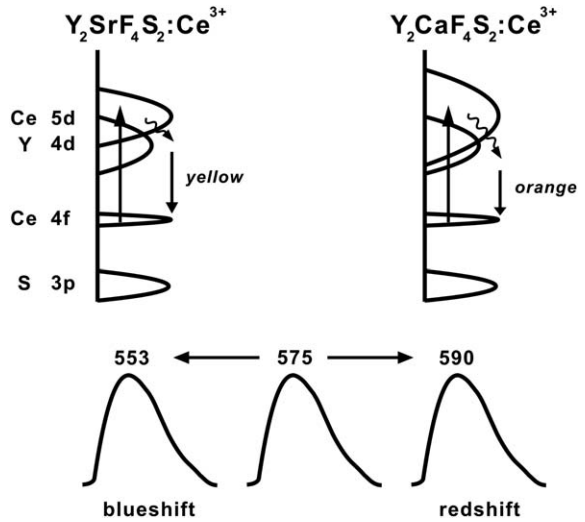

Fig. 8 A plausible mechanism of electronic transition in $Y_2CaF_4S_2:Ce^{3+}$ and $Y_2SrF_4S_2:Ce^{3+}$ system. The arrows represent the electronic transitions from Ce(4f) to Ce(5d) and photoemission, respectively.

parameters for YCFS:Ce^{3+}, YCSFS-y:Ce^{3+} (y = 0.1, 0.25, 0.5, and 0.75), and YSFS:Ce^{3+} as refined from the cell refinement are presented (see Fig. S2 in the ESI†). With the same introduction of Ce^{3+}, the a-axis, c-axis and the average interatomic distances of Ce–S and Ce–F increase due to the Ca replacement of Sr in $Y_{1.98}Ce_{0.02}Ca_{1-y}Sr_yF_4S_2$. Fig. 6 shows the excitation and emission bands of fluorosulfide phosphors. The excitation spectrum of the YCSFS-0.5:Ce^{3+} sample can be well excited by the blue light (461 nm) and the emission of the phosphor shifts to 575 nm. On the other hand, the emission intensity of the phosphors was enhanced as the Sr^{2+} ion concentration increased. The spectral and structural parameters were summarized in Table 3. The quantum efficiency (QE) of the synthesized phosphor is obtained at room temperature. The QE of $Y_{1.98}Ce_{0.02}Ca_{1-y}Sr_yF_4S_2$ increases as expected from y = 0 to 1 and reaches 15.9% to the maximum of 31.1% under excitation at 470 to 440 nm, respectively. Furthermore, the decay curve of YCFS:Ce^{3+}, YCSFS-y:Ce^{3+} (y = 0.1, 0.25, 0.5, and 0.75) and YSFS:Ce^{3+} phosphors excited at 440–470 nm and monitored at 553–590 nm are shown (see Fig. S3 in the ESI†). The corresponding luminescence decay can be calculated to be 25.7, 32.1, 39.1, 45.5, and 51.82 ns using the first-order exponential equation. These results illustrate that the Ce^{3+} ions occupy only the Y site in YCFS, YCSFS-y (y = 0.1, 0.25, 0.5, and 0.75), and YSFS host. As a result, the absorption band of YCSFS-y:Ce^{3+} matches well with the emission of the blue LED chip; thus, fluorosulfide phosphors show the potential as a promising candidate for solid-state lighting compared to commercial CaS:Ce^{3+}.

Band structure and density of states

The use of the first principle density functional theory (DFT) in understanding the electronic structure of the host lattice has been receiving much recent attention.[46,47] It is well-known that to avoid the transformation of the crystal structure, most of the studies focused on undoped host and minor substitution system. In the present work, we have attempted to examine the energy levels of the Ce^{3+} ion by means of totally substituting Y^{3+} with a Ce^{3+} ion. Here, we consider two different systems including YCFS, YSFS, $Ce_2CaF_4S_2$ (CeCFS), and $Ce_2SrF_4S_2$ (CeSFS) in an attempt to understand the variation of crystal field strength and interatomic interactions in our host compounds. Fig. 7 shows the total (DOS) and partial (PDOS) density of states and the projected DOS curves for (a) YCFS, (b) YSFS, (c) CeCFS, and (d) CeSFS, respectively. As indicated in the DOS curve of the YCFS model, the contribution of electronic states near the highest valence bands (VBs) is dominated by the S(3p) orbital, with a minor F(2p) orbital. Meanwhile, the lowest conduction band (CB) is mainly dominated by the Y(4d) orbital. The calculated electronic structure indicates that a direct charge transfer may occur not only from the S(3p) to the Y(4d) orbital but also from the F(2p) to the Y(4d) orbital. The orbital contributions observed in the DOS plot of the YSFS model are almost the same with the only difference noted in the distributed location of the Sr atom. As both the S(3p) and F(2p) orbitals are located similarly to Y(4d) in the VB (about −5 to −3 eV and CB about 1 to 3 eV), interactions within these orbitals give significant contribution to the Y band. These results demonstrate that these overlaps correspond to Y–S and Y–F bonding interactions. Hence, the anionic ligands play a very important role in advancing the ligand-to-metal charge transfer (LMCT) effectively to the Y^{3+} ion, which is in agreement with the strong Ce^{3+} photoluminescence properties as observed in our PL results. The DOS curve of the CeCFS model shows another different case in studying the charge transfer mechanism; here, the Y atoms are all replaced by dopant Ce atoms. The contributions of the electronic state around the VB close to 0 eV are dominated by a sharp localized Ce(4f) orbital and a Ce(5d) orbital around the CB. The charge transfer may occur mostly from the Ce(4f) to the Ce(5d) orbital. In addition, the DOS plot of CeSFS is essentially similar to that of CeCFS and the charge transfer in CeSFS is also made of Ce(4f) and Ce(5d) orbitals. The results suggest that the contribution of band gap is consistent with the lowest absorption

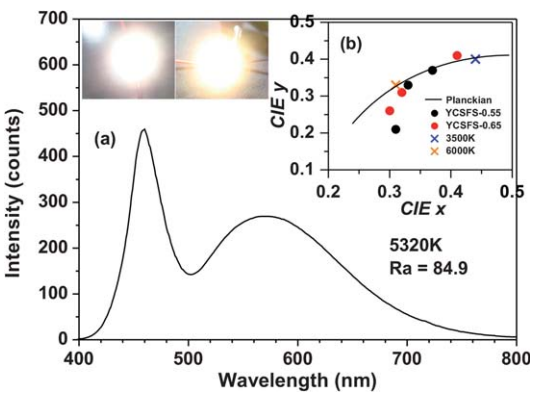

Fig. 9 (a) EL spectra of a phosphor-converted white LED using $Y_{1.98}Ce_{0.02}Ca_{0.45}Sr_{0.55}F_4S_2$ as the conversion phosphor with blue chip (460 nm). (b) Variation in CIE chromaticity coordinates as a function of the fraction of phosphor/resin used. The inset shows the photos of $Y_{1.98}Ce_{0.02}Ca_{0.35}Sr_{0.65}F_4S_2$/blue chip (left) and $Y_{1.98}Ce_{0.02}Ca_{0.45}Sr_{0.55}F_4S_2$/blue chip (right) taken under forward bias current. The Planckian locus line and the points corresponding to color temperatures of 6000 and 3500 K are indicated.

Table 4 Chromaticity and optical parameters for phosphor-converted white LED with $Y_{1.98}Ce_{0.02}Ca_{0.45}Sr_{0.55}F_4S_2$ and $Y_{1.98}Ce_{0.02}Ca_{0.35}Sr_{0.65}F_4S_2$ as the conversion phosphor layer

Sample	Phosphor/resin weight ratio (%)	CIE *x*	CIE *y*	CCT/K	CRI/*Ra*	Luminous efficacy/lm W^{-1}
YCSFS-0.55:Ce^{3+}	5	0.31	0.21	6962	83.5	19.8
	10	0.33	0.33	5320	84.9	16.7
	15	0.37	0.37	4201	81.6	14.2
YCSFS-0.65:Ce^{3+}	5	0.3	0.26	8772	83.9	29.18
	10	0.32	0.31	5812	85	27
	15	0.41	0.41	3511	74	17.43

energy. In particular, the tendency in calculated value of band gap for CeCFS and CeSFS is close to the tendency obtained for $Ca_{1-x}Sr_xS:Eu^{2+}$.[48] In CaS and SrS host lattices, the energy gaps are 4.3 and 4.41 eV due to the dissimilarity in ionic radius between Ca^{2+} and Sr^{2+}.[49] In the CeCFS and CeSFS system, the larger ionic radius of the Sr^{2+} ion introduces the increment of the volume, thus changing the bond length between the Ce^{3+} and S^{2-} ions and the shrinkage of Ce(5d) was observed in the DOS plot. With the decrement of crystal field strength in CeSFS, the Ce 5d levels split smaller and thus generate a higher band gap. These changes are in agreement with the experimental results, where we find that the excited wavelength of the YSFS:Ce^{3+} is found to have a blueshift. A brief scheme for the luminescent mechanism (see Fig. 8), in which electrons are excited from VB *via* Ce(4f) to CB *via* Ce(5d) in YCFS:Ce^{3+} and YSFS:Ce^{3+}, and then through the nonradiative Stoke shift relaxation to the lower stage is shown. In the last step, the electron goes back to the VB; such a process may result in luminescence or it may be lost thermally.

Performance of LED devices based on $Y_{1.98}Ce_{0.02}(Ca_{1-y}Sr_y)F_4S_2$ phosphors

Currently, using a binary complementary color system has the benefits regarding light quality, *i.e.*, high luminous efficacy, simple packaging fabrication, and controllable uniform phosphor property. To demonstrate the potential of $Y_{1.98}Ce_{0.02}Ca_{1-y}Sr_yF_4S_2$ for a phosphor-converted white LED application, the YCSFS-0.55 and YCSFS-0.65 phosphors were then utilized to fabricate LED devices with 460 nm LED chips, as illustrated in Fig. 9. When excited by a blue chip, the whole visible spectral region can be obtained from a blue emission from the LED chip and a broad yellow emission from the YCSFS-0.55 phosphor. With the increasing ratio of the encapsulant phosphor powder, the correlating color temperatures (CCT) of this dichromatic white LED were determined from 6962 to 4201 K. The Commission International de l'Eclairage (CIE) chromaticity coordinates were also obtained from (0.31, 0.21) to (0.37, 0.37). The detailed CCT and CRI of the LED devices using YCSFS-0.55 and YCSFS-0.65 phosphors and the corresponding luminous efficiencies are shown in Table 4. Compared with the white LED using a conventional YAG:Ce^{3+} phosphor having CRI values in the range from 70 to 75 and a color temperature of 6900 K, the generated dichromatic white light in this work possesses rather improved properties, higher CRI and lower color temperature. Given that the overall device performance depends on numerous factors starting with the phosphor manufacturing issues, the efficiency of the LED chip, the fabrication processes and so forth, we believe that the white LED performance can be still further enhanced by the optimization of the device structure.

Conclusion

In summary, a new viable yellow-emitting fluorosulfide phosphor with chemical composition of $Y_{2-x}Ce_xCa_{1-y}Sr_yF_4S_2$ ($x = 0$, 0.01, 0.02, 0.04 and 0.06; $y = 0$, 0.1, 0.25, 0.5, 0.75 and 1) were synthesized and studied. The overall luminescence performances (*i.e.*, PL intensity, quantum efficiency, thermal-quenching behavior, and its application in LED fabrication) were investigated. The detailed crystal structure and density of states calculation were also presented. The preliminary studies show that this novel yellow phosphor is excitable over a broad range from UV to blue light, and its emission can be adjusted from yellow to orange by changing Sr^{2+} ions ratio. Applying $Y_{1.98}Ce_{0.02}Ca_{0.45}Sr_{0.55}F_4S_2$ phosphor on blue chip, we can obtain a warm white LED device with a high CRI value of 85 and a CCT value of 5320 K. With the interesting tunable emission property, $Y_2CaF_4S_2:Ce^{3+}$ phosphor has great application potential as a potential candidate for white light solid-state lighting, especially for generation of warm white-light.

Acknowledgements

This research was supported by National Science Council of Taiwan (ROC) under contract no. NSC98-2113-M-009-005-MY3. We thank Dr Ming-Yang Chung for assistance in the helpful suggestion.

References

1 P. Walterett, O. Brandt, A. Trampert, H. T. Grahn, J. Menniger, M. Ramsteiner, M. Reiche and K. H. Ploog, *Nature*, 2000, **406**, 865.
2 J. M. Phillips, M. E. Coltrin, M. H. Crawford, A. J. Fischer, M. R. Krames, R. Mueller-Mach, G. O. Mueller, Y. Ohno, L. E. S. Rohwer, J. A. Simmons and J. Y. Tsao, *Laser Photonics Rev.*, 2007, **1**, 307.
3 S. Pimputkar, J. S. Speck, S. P. Denbaars and S. Nakamura, *Nat. Photonics*, 2009, **3**, 180.
4 V. Bachmann, C. Ronda and A. Meijerink, *Chem. Mater.*, 2009, **21**, 2077.
5 A. B. Munoz-Garcia and L. Seijo, *J. Phys. Chem. A*, 2011, **115**, 815.
6 R. Mueller-Mach, G. Mueller, M. R. Krames, H. A. Höppe, F. Stadler, W. Schnick, T. Juestel and P. Schmidt, *Phys. Status Solidi A*, 2005, **202**, 1727.
7 M. R. Krames, O. B. Shchekin, R. Mueller-Mach, G. O. Mueller, L. Zhou, G. Harbers and M. Craford, *J. Disp. Technol.*, 2007, **3**, 160.

8 A. A. Setlur, W. J. Heward, M. E. Hannah and U. Happek, *Chem. Mater.*, 2008, **20**, 6277.
9 P. F. Smet, A. B. Parmentier and D. Poelman, *J. Electrochem. Soc.*, 2011, **158**, R37.
10 D. Jia and X. Wang, *Opt. Mater.*, 2007, **30**, 375.
11 C. Guo, D. Huang and Q. Su, *Mater. Sci. Eng., B*, 2006, **130**, 189.
12 R. Mueller-Mach, O. Mueller-Gerd, M. R. Krames and T. Trottier, *IEEE J. Sel. Top. Quantum Electron.*, 2002, **8**, 339.
13 H. Wu, X. Zhang, C. Guo, J. Xu, M. Wu and Q. Su, *IEEE Photonics Technol. Lett.*, 2005, **17**, 1160.
14 P. F. Smet, K. Korthout, J. E. Van Haecke and D. Poelman, *Mater. Sci. Eng., B*, 2008, **264**, 146.
15 Y.-R. Do, K.-Y. Ko, S.-H. Na and Y.-D. Huh, *J. Electrochem. Soc.*, 2006, **153**, H142.
16 V. Petrykin, M. Okube, H. Yamane, S. Sasaki and M. Kakihana, *Chem. Mater.*, 2010, **22**, 5800.
17 P. Dorenbos, *J. Lumin.*, 2000, **91**, 155.
18 S. Gai, P. Yang, X. Li, C. Li, D. Wang, Y. Dai and J. Lin, *J. Mater. Chem.*, 2011, **21**, 14610.
19 Y. Q. Li, N. Hirosaki, R.-J. Xie, T. Takeda and M. Mitomo, *Chem. Mater.*, 2008, **20**, 6704.
20 T. Schleid, *Z. Anorg. Allg. Chem.*, 2000, **626**, 2429.
21 A. Demourgues, A. Tressauda, H. Laronzea and P. Macaudiere, *J. Alloys Compd.*, 2001, **323**, 223.
22 H. Grossholz, I. Hartenbach, G. Kotzyba, R. Pottgen, H. Trill, B. D. Mosel and T. Schleid, *J. Solid State Chem.*, 2009, **182**, 3071.
23 Y.-C. Wu, D.-Y. Wang, T.-M. Chen, C.-S. Lee, K.-J. Chen and H.-C. Kuo, *ACS Appl. Mater. Interfaces*, 2011, **3**, 3195.
24 Y.-C. Wu, Y.-C. Chen, D.-Y. Wang, C.-S. Lee, C.-C. Sun and T.-M. Chen, *J. Mater. Chem.*, 2011, **21**, 15163.
25 A. C. Larson and R. B. Von Dreele, *General Structure Analysis System (GSAS)*, Los Alamos National Laboratory Report LAUR 86-748, Los Alamos National Laboratory, Los Alamos, NM, 1994.
26 O. K. Andersen, *Phys. Rev. B: Solid State*, 1975, **12**, 3060.
27 O. Jepsen and O. K. Andersen, *Z. Phys. B: Condens. Matter*, 1995, **97**, 35.
28 U. Von Barth and L. Hedin, *J. Phys. C: Solid State Phys.*, 1972, **5**, 1629.
29 R. D. Shannon, *Acta Crystallogr., Sect. A: Cryst. Phys., Diffr., Theor. Gen. Crystallogr.*, 1976, **32**, 751.
30 N. Kodama, M. Yamaga and B. Henderson, *J. Appl. Phys.*, 1998, **84**, 5820.
31 C. I. Aguirre, E. Reguera and A. Stein, *ACS Appl. Mater. Interfaces*, 2010, **2**, 3257.
32 P. Dorenbos, *J. Lumin.*, 2000, **91**, 91.
33 G. Denis, X. Rocquefelte, P. Deniard, M. H. Whangbob and S. Jobic, *J. Mater. Chem.*, 2009, **19**, 9170.
34 P. Dorenbos, *J. Lumin.*, 2002, **99**, 283.
35 A. A. Setlur, E. V. Radkov, C. S. Henderson, J. H. Her, A. M. Srivastava, N. Karkada, M. S. Kishore, N. P. Kumar, D. Aesram, A. Deshpande, B. Kolodin, L. S. Grigorov and U. Happek, *Chem. Mater.*, 2010, **22**, 4076.
36 W. B. Im, S. Brinkley, J. Hu, A. Mikhailovsky, S. P. DenBaars and R. Seshadri, *Chem. Mater.*, 2010, **22**, 2842.
37 G. Blasse, *Philips Res. Rep.*, 1969, **24**, 131.
38 D. L. Dexter, *J. Chem. Phys.*, 1953, **21**, 836.
39 L. G. Van Uitert, *J. Electrochem. Soc.*, 1963, **110**, 46.
40 L. Ozawa, H. Forest, P. M. Jaffe and G. Ban, *J. Electrochem. Soc.*, 1971, **118**, 482.
41 G. Li, D. Geng, M. Shang, C. Peng, Z. Cheng and J. Lin, *J. Mater. Chem.*, 2011, **21**, 13334.
42 B. Henderson and G. F. Imbush, *Optical Spectroscopy of Inorganic Solids*, Clarendon, Oxford, 1989.
43 G. Blasse, *Luminescence of Inorganic Solids*, Plenum Press, New York, 1978.
44 R.-J. Xie, N. Hirosaki, N. Kimura, K. Sakuma and M. Mitomo, *Appl. Phys. Lett.*, 2007, **90**, 191101.
45 C.-H. Huang and T.-M. Chen, *Inorg. Chem.*, 2011, **50**, 5125.
46 C.-C. Lin, Z.-R. Xiao, G.-Y. Guo, T.-S. Chan and R.-S. Liu, *J. Am. Chem. Soc.*, 2010, **132**, 3010.
47 C. Braun, M. Seibald, S. L. Borger, O. Oeckler, T. D. Boyko, A. Moewes, G. Miehe, A. Tucks and W. Schnick, *Chem.–Eur. J.*, 2010, **16**, 9646.
48 M. Nazarov and C. Yoon, *J. Solid State Chem.*, 2006, **179**, 2529.
49 T. Shosaku, *J. Lumin.*, 1988, **40–41**, 20.

